Flow-Driven Resonant Energy Systems

Alessandro Alabastri*

Department of Electrical and Computer Engineering, Rice University, 6100 Main Street, Houston, Texas 77005, USA

(Received 9 June 2020; revised 30 July 2020; accepted 4 August 2020; published 17 September 2020)

Here we provide a physical and mathematical framework for the description of flow-driven oscillators. These oscillators, differently from frequency-driven harmonic systems, are based on countercurrent mass flows and thermal-energy exchange. We describe this class of oscillators through two countercurrent fluids separated by a heated conductive medium. We show how this configuration embeds the essential elements of harmonic oscillators, such as resonance condition, periodic orbits, and quality factor or decay time. The key advantage of recognizing flow-driven systems as oscillators lies in the possibility to engineer them according to the properties of resonant systems and utilize them to control their temperature, maximize the stored energy, or coupling them in networks. We report examples of simple configurations at their resonant condition, enhancing both thermal energy and decay time by factors larger than 10. We finally show two flow-driven oscillators coupled in series, featuring a reconfigurable internal temperature distribution, depending on the selected resonant condition.

DOI: 10.1103/PhysRevApplied.14.034045

I. INTRODUCTION

Oscillations can be described as temporal evolutions of quantities, whose values repeat periodically [1]. Periodic phenomena are ubiquitous in nature, from planets rotation and revolution [2], to heartbeats of vertebrates and circadian rhythms [3], to brainwaves [4] or electromagnetic fields [5]. Among oscillating systems, driven oscillators are of particular interest as their resonant behavior can be externally controlled for many applications, such as resonant circuits [6], optical resonances [7], or micromechanical resonators [8]. Resonant systems are usually driven by frequency-dependent inputs but, recently, flow-rate-based thermal resonators have also been proposed [9]. However, a formal description of such resonant heat transfer is lacking. Here we show how flow-driven systems can be formally described as oscillating units.

Oscillating systems can be visualized as state variables generating spiral trajectories or closed loops in the phase plane [10]. Such state variables can represent many different phenomena: *amplitude* and *velocity* for a simple pendulum [11], *prey* and *predators* in species fluctuations [12], and even *interpersonal feelings* in complex love stories [13,14]. Oscillations identified by two state variables (v_1 and v_2) can be characterized through the properties of the associated two-dimensional dynamical system that, if linear, can be studied by analyzing the coupled equations [10]:

$$\begin{pmatrix} \dot{v}_1 \\ \dot{v}_2 \end{pmatrix} = \begin{pmatrix} a & b \\ c & d \end{pmatrix} \begin{pmatrix} v_1 \\ v_2 \end{pmatrix}. \tag{1}$$

This system has eigenvalues $\lambda_{1,2} = \left(\zeta \pm \sqrt{\zeta^2 - 4\Delta}\right)/2$ with $\zeta = \lambda_1 + \lambda_2 = a + d$ and $\Delta = \lambda_1\lambda_2 = ad - bc$, and its qualitative behavior can be inferred from Δ and ζ values. In particular, if $\Delta > 0$, $\zeta < 0$ and $\zeta^2 - 4\Delta < 0$ the eigenvalues are complex, the trajectories are spirals with period $T = 2\pi/\omega_0$ and angular frequency $\omega_0 = \left(\sqrt{4\Delta - \zeta^2}\right)/2$ and the equilibrium point $(v_1 = 0, v_2 = 0)$ is stable. One classical example is a *RLC* circuit [see Fig. 1(a)] where an oscillating input voltage, $V_{\text{in}}(\omega)$, drives the system by inducing its energy to oscillate between the inductor and the capacitor with resonance at $\omega_0 \cong 1/\sqrt{LC}$.

The concept applies to many systems, such as, for instance, metallic nanoparticles [Fig. 1(a)], where conductive electrons can be driven by the electric field, $E_{\text{in}}(\omega)$, of an electromagnetic wave. For spherical particles in vacuum, the amplitude of electron oscillation is maximized at $\omega_0 \cong \omega_p/\sqrt{3}$, where ω_p is the plasma frequency of the metal [15]. Radiation and dissipation losses are captured, by damping terms, Γ_{rad} and Γ_{diss}, respectively.

These two examples share many similarities and, in fact, metallic nanostructures can sometimes be approximated by *LC* circuits [16]. Importantly, in both cases, the external driving input is a frequency-dependent signal and the stored energy alternates between physical quantities such as electric and magnetic fields.

*alessandro.alabastri@rice.edu

II. FREQUENCY VERSUS FLOW-DRIVEN OSCILLATORS

Here we introduce another class of oscillators, which, differently from time and frequency inputs, are controlled by fluid flow rates. To illustrate the concept, we choose a prototypical system [see Fig. 1(b)] composed of two fluids in countercurrent configuration with opposite flow rates, Q_0 and Q_{in}, separated by a thin conductive medium heating both fluids with power intensity I_s. The input thermal energy can be lost through the flow outlets (Γ_{out}) or released towards the environment (Γ_{env}). We let Q_{in} and I_s be easily controllable, thus representing external drivers, while we assume Q_0 and the rest of the geometrical and material parameters are fixed. The power intensity is, therefore, ultimately controlled by the flow rate $I_s(Q_{in})$.

We demonstrate how this thermofluidic system exhibits oscillatory behaviors and resonant conditions by tuning the flow-rate controlled external input $I_s(Q_{in})$. We show how thermal advection and conduction are at the base of the oscillating mechanism where heat fluxes are periodically exchanged between the two flows, storing thermal energy in the fluids and reaching a maximum for $Q_{in} \sim Q_0$, as in a resonant condition. More details on the analogy among the examples of Fig. 1 are reported in Appendix A.

Heat transfer between fluids in similar systems has been previously studied for many applications, such as heat exchangers [17–21] or membrane distillation [22–24]. However, the oscillating behavior has been so far overlooked probably because, in more common applications, the regions where fluids are heated (energy input) and interact (energy exchange) are usually separated in space and/or time. However, applications with colocalized power input and heat exchange are also of major interest [25,26]. One example is nanoparticle-assisted solar-driven membrane distillation, where nanoparticles act as efficient light-heat converters [27–29] and transfer heat in parallel to the desalination process [30,31]. In fact, resonant heat transfer has been recently proposed as a thermal-energy recovery method to boost the efficiency of light-driven desalination [9] but a comprehensive formal framework was not provided.

III. HEAT TRANSFER DYNAMICS IN FLOW-DRIVEN OSCILLATORS

A. Periodic oscillations and resonances

To provide a general context to flow-driven thermal oscillators, we examine the system introduced in Fig. 1, as shown in Fig. 2(a). Two thermally insulated parallel countercurrent streams, Q_1 and Q_2, (entering the system at temperature T_{amb}), flow in channels 1 and 2 (length L, thickness w, and width D) with homogeneous velocities $u_1 = Q_1/A$ and $u_2 = Q_2/A$ (with $A = wD$ the cross section of the channels). The flows are separated by a thin nonpermeable conductive layer and are heated by a constant heat source of intensity I_s. The channels exchange heat fluxes, I_{21} and I_{12}, depending on their relative temperature difference, $I_{ji} = h\Delta T_{ji}$, and the fluid streams leave the system through the channel outlets. The parameter h is a heat-transfer coefficient, which, for simplicity, includes the thermal properties of both the conductive layer and the fluids.

We assume that advection occurs only in the direction parallel to the channels (x) and that temperature is homogenous along the thickness of the channels (y). This simplified problem reduces to two one-dimensional (1D) systems and, applying the continuity equation (see

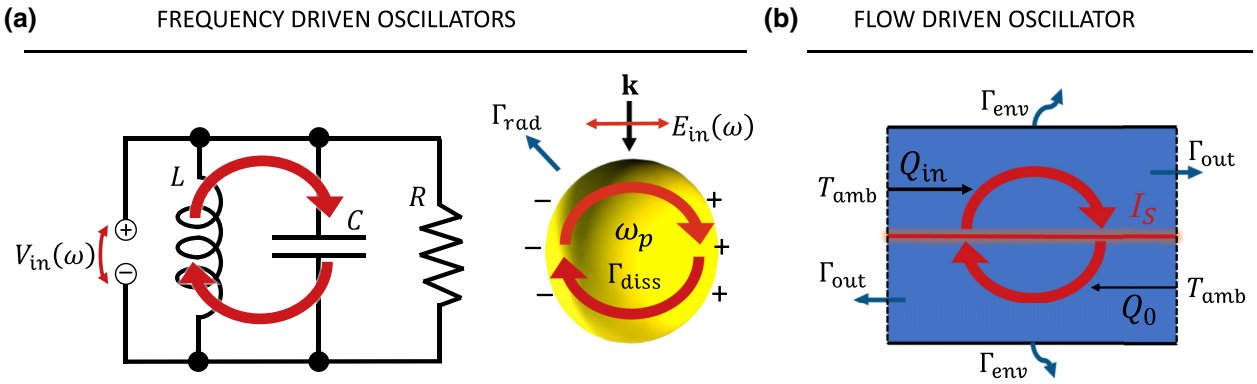

FIG. 1. Examples of frequency-driven and flow-driven oscillators. (a) A parallel *RLC* circuit and a plasmonic metallic nanoparticle. The *RLC* circuit is driven by an oscillating electric potential, $V_{in}(\omega)$; the metallic nanoparticles by an oscillating electric field, $E_{in}(\omega)$ (of an electromagnetic wave with wave vector **k**). (b) A thermofluidic system, prototype of flow-driven thermal oscillators; the thermofluidic system (represented by a flow rate Q_0) is driven by a countercurrent heated flow rate, $I_s(Q_{in})$. Losses are represented by a resistance, R; internal dissipation, Γ_{diss}; reirradiation, Γ_{rad}; flow outlets, Γ_{out}; and environmental heat exchanges, Γ_{env}, for the three systems, respectively.

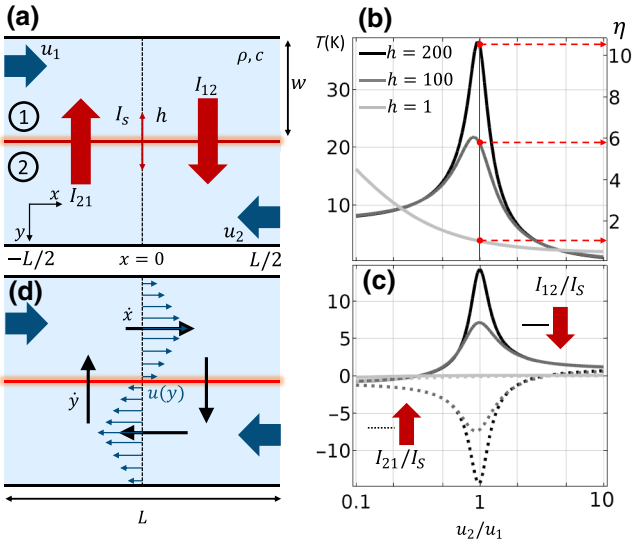

FIG. 2. (a) Scheme of a flow-driven oscillator composed of two coupled fluidic channels of length L and thickness w. Two countercurrent fluids (1 and 2), with density ρ and specific heat c, enter the system along the x direction with homogeneous velocity u_1 and u_2, respectively. The channels are separated by a thin layer acting as a common heating source $I_s = 50$ W/m^2 characterized by a generalized heat-transfer coefficient h. The channels exchange heat across the interfacial layer through I_{21} and I_{12} for $x < 0$ and $x > 0$, respectively. (b) System average temperature increase (left axis) and decay time (right axis) depending on (u_2/u_1) for different $h = 1, 100, 200$ W/(m^2 K) from light to dark gray color, respectively. η_{res} as from Eq. (7) is shown by red arrows. (c) Average transferred heat fluxes I_{12} and I_{21} normalized to I_s, in channels 1 (solid) and 2 (dashed) depending on (u_2/u_1) for different $h = 1, 100, 200$ W/(m^2 K) from light to dark gray color, respectively. The system has $L = 0.5$ m and $w = 1$ mm. (d) Scheme of the interacting channels where the velocity field $u(y)$ (blue thin arrows) has a linear triangular shape. The rate of change of heat fluxes, $\dot{x}$ and $\dot{y}$, along x and y, respectively, are symbolized by black thin arrows.

Appendix B), we obtain

$$\begin{aligned}\frac{\partial T_1(x)}{\partial x} &= \frac{1}{\varphi|u_1|}\big[-h\Delta T(x) + I_s\big],\\ \frac{\partial T_2(x)}{\partial x} &= \frac{1}{\varphi|u_2|}\big[h\Delta T(x) + I_s\big],\end{aligned} \tag{2}$$

with $\Delta T(x) = T_1(x) - T_2(x)$, $T_1(-L/2) = T_2(L/2) = T_{\text{amb}} = 20\,^\circ$C, and $\varphi = \rho c w$, with ρ, c the density and the specific heat of the fluid. The closed form analytical solutions of Eq. (2) and the temperature profiles are reported in Appendices C and D.

In Fig. 2(b) we plot the average system temperature increase, $\Delta\tilde{T} = (1/2L)\left\{\int_{-L/2}^{L/2}\left[T_1(x) + T_2(x) - 2T_{\text{amb}}\right]dx\right\}$, (left axis) of the system depending on the ratio, u_2/u_1, for different values of h, with water as fluid. A peak in temperature increase, and thus a maximum in the stored thermal energy $H \propto \rho c\tilde{T}$, is reached for matched velocities and large heat-transfer coefficients. This is explained by considering the average heat fluxes defined as $I_{12} = -(2/L)\int_0^{L/2} h\Delta T(x)\,dx$ and $I_{21} = (2/L)\int_{-L/2}^{0} h\Delta T(x)\,dx$ exchanged between the channels, from 1 to 2 if $x > 0$ and from 2 to 1 if $x < 0$. Similarly to temperature maxima, the exchanged heat fluxes, with opposite signs, exhibit a peak for $u_2/u_1 \sim 1$ and large h as shown in Fig. 2(c).

To visualize the oscillating behavior, we consider the overall heat dynamics within the coupled channels.

To model the heat dynamics, we reintroduce the y coordinate to indicate the heat transfer across the channels and we seek the conditions such that the heat trajectories in the x-y plane are represented by circular paths and spirals, fingerprints of periodic (oscillating) solutions. To this end, we consider a probe in our system dragged by a vector field $(\dot{x}, \dot{y})$, proportional to the magnitude of heat fluxes. Coherently with previous assumptions (advection along x and conduction along y) we can write [see Fig. 2(d)]

$$\begin{cases}\dot{x} = \begin{cases}\rho c u_1 T_1(x), & y > 0\\ -\rho c u_2 T_2(x), & y < 0\end{cases}\\ \dot{y} = -h\Delta T(x).\end{cases} \tag{3}$$

The trajectories for $u_2 > u_1$, $u_2 \sim u_1$, and $u_2 < u_1$ are shown in Figs. 3(a)–3(c), superimposed to the heat vector field and system geometry. At matched velocities, $u_2 \sim u_1$, the heat is confined within the system for a longer time, as expressed by the more compact trajectories.

We then examine the linearized version of the system of Eq. (3) for $u_2 \sim u_1$, to adopt the matrix representation introduced in Eq. (1), from which we can obtain the parameters typical of periodic systems (see Appendices E and F):

$$\begin{pmatrix}\dot{x}\\ \dot{y}\end{pmatrix} = \begin{bmatrix}0 & \dfrac{I_s L}{w^2}\left(\dfrac{hL}{\varphi u} + 2\right)\\ -h\dfrac{2I_s}{\varphi u} & 0\end{bmatrix}\begin{pmatrix}x\\ y\end{pmatrix}. \tag{4}$$

The linearized system is formally equivalent to Eq. (1) with coefficients $a = 0$, $b = (I_s L/w^2)\big(hL/\varphi u + 2\big)$, $c = -h(2I_s/\varphi u)$, $d = 0$ and with $\zeta = 0$, $\Delta = h(2I_s^2 L/\varphi u)(1/w^2)\big(hL/\varphi u + 2\big)$. Therefore, the eigenvalues are purely imaginary:

$$\lambda_{1,2} = \pm i\omega_0 = \pm i\frac{I_s}{w}\sqrt{\frac{2hL}{\varphi u}\left(\frac{hL}{\varphi u} + 2\right)} \tag{5}$$

and the system dynamics is described by closed orbits. The equilibrium point, $(0, 0)$, is a center and the trajectories are periodic with period $T = 2\pi/\omega_0$ as shown in

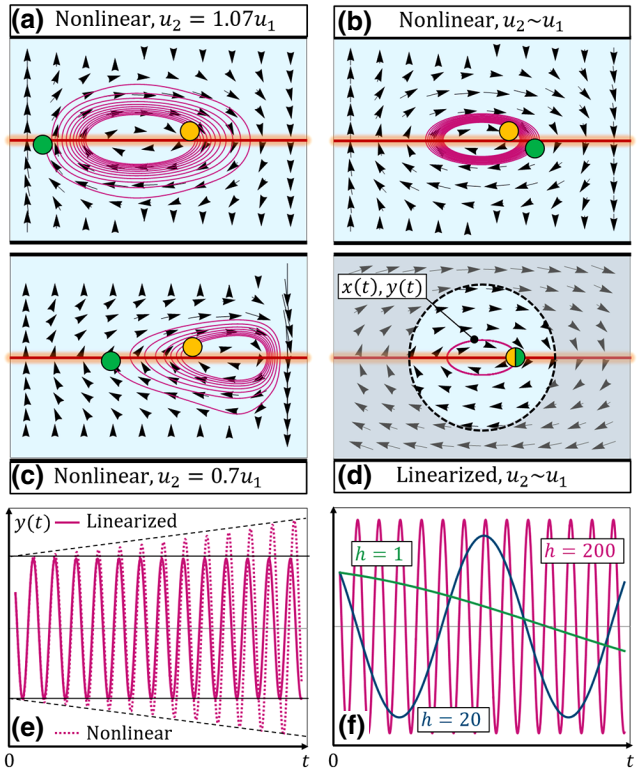

FIG. 3. (a)–(d) Time trajectory of a massless probe, dragged by the heat-flux field, starting at $x_0 = L/8$ and $y_0 = w/10$ (dark yellow circle) until an arbitrary time, $t = 40$ μs (green circle) for $u_2 = 1.07u_1$ (a); $u_2 \sim u_1$ (b); $u_2 \sim 0.7u_1$ (c). Panel (d) illustrates the linearized system shown in (b). (e) Value of the coordinate $y(t)$ over time for the case $u_2 \sim u_1$ in the linearized (solid) and nonlinear (dashed) model. (f) Value of the coordinate $y(t)$ over time for the case $u_2 \sim u_1$ in the linearized model for different $h = 1, 20, 200$ W/(m^2 K), green, blue, and magenta lines, respectively.

Fig. 3(d). Overall, ω_0 expresses the frequency of heat oscillation per unit of energy density and is expressed in [J/(s m^3)] or [W/m^3]. In Fig. 3(e) we plot the vertical heat-flux trajectory $y(t)$ versus time for both the linearized and the complete nonlinear system. Since no dissipation is considered in the linearized case ($\zeta = a + d = 0$), heat is exchanged indefinitely and the trajectory is confined relatively close to the origin. In the nonlinear case, the trajectories are ruled by Eq. (3): the unstable spirals pull the probe from the origin [Figs. 3(a)–3(c)] towards the outlets and the oscillation amplitude increases with time [Fig. 3(e), dotted line]. More details in Appendix G. The proximity of heat fluxes to the outlets increases advection losses (heat is carried out of the system by the flows) and limits thermal-energy accumulation, ensuring the stability of the system. See Appendix H for further details on the effect of system perturbations. The role of the heat-transfer coefficient is shown in Fig. 3(f) for the linearized case. The oscillation frequency, ω_0, increases for larger h: 1, 20 and 200 W/(m^{2}K), in accordance to the eigenvalues of Eq. (5).

B. Thermal-energy accumulation and decay time

To quantify the resonant effect, we introduce the average permanence time, τ, of thermal-energy increase in the whole system defined as $\Delta H = \rho c w \int_{-L/2}^{L/2} \left[T_1(x) + T_2(x) - 2T_{\text{amb}}\right] dx$. In steady state, input power equals losses and $\tau = \Delta H/(I_0 L)$. τ relates to the decay time and to the quality factor of a resonator, Q_f, as $\tau \propto Q_f$. By evaluating τ at resonance, τ_{res}, we find

$$\tau_{\text{res}} = \frac{1}{I_s L} \lim_{Q_1 \to Q_2} \Delta H = \frac{L}{u}\left(1 + \frac{hL}{3\varphi u}\right). \tag{6}$$

τ_{res} is composed of two terms: a *dwell* time (L/u) and an *interaction* ($hL^2/3\varphi u^2$) time. The dwell time, $\tau_0 = \tau_{\text{res}}|_{h\to 0} = L/u$, indicates the average time it takes the fluid to go through the channel. The *interaction* time is due to the interaction between the channels and effectively prevents heat "escaping" from the system. We can define a time-decay enhancement, $\eta = \tau/\tau_0$, which at resonance becomes

$$\eta_{\text{res}} = \frac{\tau_{\text{res}}}{\tau_0} = 1 + \tau_0 \frac{h}{3\varphi}. \tag{7}$$

The calculated η is plotted against u_1/u_2 in Fig. 2(b) (right axis), consistently with the curves of $\Delta\tilde{T}$. While Eq. (7) is accurate only when external losses and further nonlinear effects can be neglected, it provides a roadmap for the design of thermofluidic resonators. The comparison between η and η_{res} is shown by the red arrows in Fig. 2(b). Thermal energy can be enhanced up to 10 times in our example. η_{res} well matches η curves when $u_1/u_2 \sim 1$, especially for large h where the resonance condition becomes closer to $u_1/u_2 \sim 1$, for which the expression of η_{res} is obtained. The impact of losses and fluid thermal conductivity for a more realistic system are reported in Appendices I and J. The comparison between water and a liquid metal (e.g., Galinstan) as candidates for the flowing fluids in the system is also reported (Appendix K). The analytical expressions currently employed in the theoretical model neglect diffusive heat transport within the channels (x direction). This simplification works well for fluids with a relatively small thermal conductivity. The case of more conductive fluids can be treated numerically.

IV. COUPLED FLOW-DRIVEN RESONATORS

By recognizing these thermofluidic systems as oscillators, we can exploit the concept of resonant condition between two channels, $Q_1/Q_2 \sim 1$, to control the spatial temperature map across multiple oscillators. This paves the way for the design and optimization of relatively complex systems with desired properties, by using such oscillators as building blocks. Let us present this idea on a relatively simple design where we introduce a horizontal thermal barrier in a channel to screen the vertical heat flux and alter the

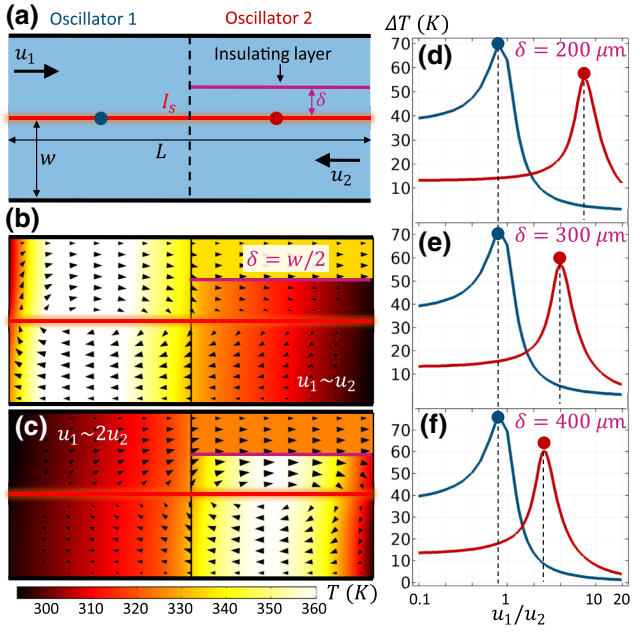

FIG. 4. Series of oscillators. (a) Two oscillators (oscillator 1, blue; oscillator 2, red) of length $L/2$, width w input velocities u_1 and u_2 are positioned in series. Oscillator 2 features an insulating layer at distance δ from the interface heating both channels with intensity I_s. The boundaries of the insulating layers feature slip-boundary conditions. The blue and red circles show the center of each oscillator. (b) Thermal map (colors) and heat-flux vector field (black arrow heads) for the case $\delta = w/2$ and $u_1 \sim u_2$. (c) Same as (b) with $u_1 \sim 2u_2$. (d) Temperature increase in the oscillator centers depending on the top channel velocities u_1 when $u_2 = 5$ mm/s and $w = 1$ mm for $\delta = 200$ μm. (e),(f) Same as (d) with $\delta = 300$ μm and $\delta = 400$ μm, respectively. Oscillators are assumed to be insulated from the environment.

resonant condition. We report a numerical example of such a configuration in Fig. 4(a) for two oscillators (1 and 2 of width w) in series where oscillator 2 features an ideal zero-thickness insulating layer at a distance δ from the interface. By fixing the flow velocity in channel 2, u_2, in Figs. 4(b) and 4(c) we show the temperature maps (colors) and heat-flux vector field (arrowheads) when $\delta = w/2$ with $u_1 = u_2$ (top) and $u_1 = 2u_2$ (bottom). The peak temperature and the spiral-like heat-flux pattern shift from left (oscillator 1) to right (oscillator 2) according to the resonant condition $u_1 = u_2$ for oscillator 1 and $u_1 = 2u_2$ for oscillator 2 (as the transported heat flux in channel 1 is halved by the thermal barrier). In Figs. 4(d)–4(f) we report the maximum temperature increase dependence on u_1 for both oscillators in the case of different thermal-barrier positions. It is now clear why, in Fig. 1, we define the general *input* of thermofluidic systems as $I_s(Q_{\text{in}})$: I_s establishes the amplitude of the maximum reached temperature and Q_{in} controls the resonant condition, upon matching with the opposite channel effective flow rate.

V. CONCLUSIONS

In conclusions, we introduce a class of thermofluidic devices, which can be regarded as thermal oscillators. Similarly to other well-known resonant systems, flow-driven oscillators feature resonant conditions and a time decay of the stored energy, which is maximized at resonance. One of the simplest configurations consists of two countercurrent flows separated by a heat source, but networks of such oscillators can be conceived. While oscillators can be found almost in any field of science and engineering, thermofluidic resonators are of extreme importance because they can be externally controlled through input heat sources and flow rates. One example of application is resonant heat transfer for solar water desalination and it is discussed in Appendix L. The resonant thermal condition is not confined to conductive heat transfer, but it can be applied to any type of heat transfer, which can be combined with convective (advective) transport. We expect the concept of resonant thermofluidic systems to find applications wherever the control of temperature plays a major role, from microfluidic devices to chemical reactor chambers.

ACKNOWLEDGMENTS

I thank Dr. L. Maserati, Dr. P. Dongare, Dr. E. Bartoli, Dr. L. Bursi, and Mr. A. Schirato for their valuable suggestions and constructive discussions. This material is based upon work supported by the National Science Foundation under Grant No. (IIP-1941227).

APPENDIX A: COMPARISON BETWEEN FREQUENCY AND FLOW-DRIVEN SYSTEMS

To provide a more detailed comparison between flow-driven and frequency-driven oscillators, in Table I below, we report their comparison in terms of input signal, resonant condition, stored energy and loss mechanisms.

APPENDIX B: SIMPLIFIED CONTINUITY EQUATION

We start by considering the change of internal energy for a Newtonian fluid [32] (described by a fluid velocity field, $\mathbf{u}$, density ρ, and specific heat c at constant pressure):

$$\rho c_p \left(\frac{\partial T}{\partial t}\right) = -\rho c\,(\mathbf{u}\cdot\nabla)\,T - (\nabla\cdot\mathbf{q}) - \tau : \nabla\mathbf{u} - p\,(\nabla\cdot\mathbf{u}) + S. \tag{B1}$$

The rate of increase of internal energy per unit volume (with ρ density and c specific heat at constant pressure) is separated into its components: convective transport, heat conduction, viscous dissipation, compression and external sources, from left to right, respectively. We now assume (i) a fluid where heat transfer by advection is dominant over

TABLE I. Comparison among the different oscillating systems in terms of their external input, resonant condition, stored energy, and dissipation (losses).

	RLC circuit	Plasmonic nanoparticle	Thermofluidic system
INPUT	Voltage: $V_{\text{in}}(\omega)$	Electric field: $E_{\text{in}}(\omega)$	Heating flow rate: $I_S(Q_{\text{in}})$
RESONANCE	$\omega_{\text{res}} \approx \sqrt{\frac{1}{LC}}$	$\omega_{\text{res}} \approx \frac{\omega_p}{\sqrt{3}}$	$Q_{\text{res}} \approx Q_0$
STORED ENERGY	$E_{\text{El+Mag}} = \frac{1}{2}\left(LI^2 + \frac{q^2}{C}\right)$	$E_{\text{EM}} = \frac{1}{2}\int \epsilon_0 E^2 d\mathbf{r}$	$E_{\text{Thermal}} = \int \rho c T d\mathbf{r}$
ENERGY LOSS RATE	$\Gamma = \frac{1}{RC}$	$\Gamma = \Gamma_{\text{rad}} + \Gamma_{\text{diss}}$	$\Gamma = \Gamma_{\text{out}} + \Gamma_{\text{env}}$

diffusion (large Peclet number, $\text{Pe} = \text{Re} \cdot \text{Pr} \gg 1$, where Re and Pr are Reynolds and Prandtl numbers, respectively), i.e., $|\nabla \cdot \mathbf{q}| \ll \left|\rho C_p \left(\mathbf{u} \cdot \nabla\right) T\right|$. This condition is satisfied even in relatively slow fluids. For example, water flowing at ambient pressure, close to ambient temperature, in approximately mm size channels at approximately cm/s velocities has $10 < \text{Re} < 100$ [31] and $10 < \text{Pr} < 100$ [33]; (ii) we neglect viscous dissipation as we do not consider large velocity gradients nor polymeric or highly viscous fluids [32] and (iii) we consider incompressible fluids. The rate of internal energy increase, then, simplifies to

$$\rho c_p \left[\frac{\partial T}{\partial t} + \left(\mathbf{u} \cdot \nabla\right) T\right] = S. \tag{B2}$$

This continuity equation is assumed throughout the manuscript and is at the base of the system of Eq. (2). In Eq. (2), the flow rates are implicitly considered countercurrent and the $|\ |$ symbols are introduced to avoid confusion about signs, even if both u_1 and u_2 are considered positive throughout this work. This choice allows us to write $T_1(x)$ and $T_2(x)$ solutions in more compact terms (see Appendix C).

APPENDIX C: ANALYTICAL SOLUTIONS FOR TEMPERATURE PROFILES

The analytical solutions for the temperature profiles, $T_1(x)$, $T_2(x)$, in the two channels are

$$\begin{cases} T_1(x) = \dfrac{e^{-\frac{\alpha(L+2x)}{2}} I_S \left\{2hLu_2 - he^{-\frac{\alpha(L-2x)}{2}}\left[e^{\alpha L}u_2\left(L-2x\right) + u_1\left(L+2x\right)\right] - \phi u_2 \Sigma\left(e^{\frac{\alpha(L+2x)}{2}} - 1\right)\right\}}{\phi h \Delta\left(u_2 - u_1 e^{-\alpha L}\right)}, \\ T_2(x) = \dfrac{e^{-\frac{\alpha(L+2x)}{2}} I_S \left\{hu_2 e^{\frac{\alpha(L+2x)}{2}}\left(L-2x\right) - u_2\left(2hL + \phi\Sigma\right) + e^{-\frac{\alpha(L-2x)}{2}} u_1\left[h\left(L+2x\right) + \phi\Sigma\right]\right\}}{\phi h \Delta\left(u_2 - u_1 e^{-\alpha L}\right)}. \end{cases} \tag{C1}$$

With $\alpha = (u_2 - u_1)/(\phi u_1 u_2)$, $\Sigma = u_1 + u_2$, $\Delta = u_2 - u_1$, $\phi = cw\rho$, $T_{\text{amb}} = 0$

At resonance, $u_1 = u_2 = u$, we have

$$\begin{cases} T_{1,u}(x) = \dfrac{I_S\left(L+2x\right)\left[h\left(L-2x\right) + 2u\phi\right]}{4u^2\phi^2} \\ T_{2,u}(x) = \dfrac{I_S\left(L-2x\right)\left[h\left(L+2x\right) + 2u\phi\right]}{4u^2\phi^2} \\ \Delta T_u(x) = \dfrac{2I_S}{\phi u}x \end{cases} \tag{C2}$$

APPENDIX D: TEMPERATURE-PROFILE DEPENDENCE ON HEAT-TRANSFER COEFFICIENT

The scheme of the coupled 1D systems is shown in Fig. 5. Quasisymmetric temperature profiles $T_1(x)$ and

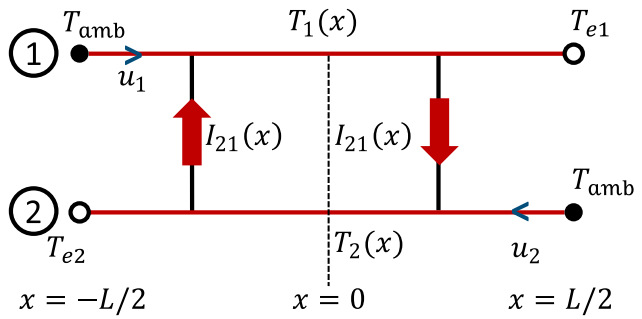

FIG. 5. System generalized as two coupled 1D systems. Flow inlets (1 and 2) are at the same fixed temperature T_{amb}. Flow outlet temperatures, T_{e1} and T_{e2}, depend on the system parameters. The space-dependent heat exchanged between the channels $I_{21}(x)$ and $I_{12}(x)$ depend on the temperature profiles of the channels $T_1(x)$ and $T_2(x)$.

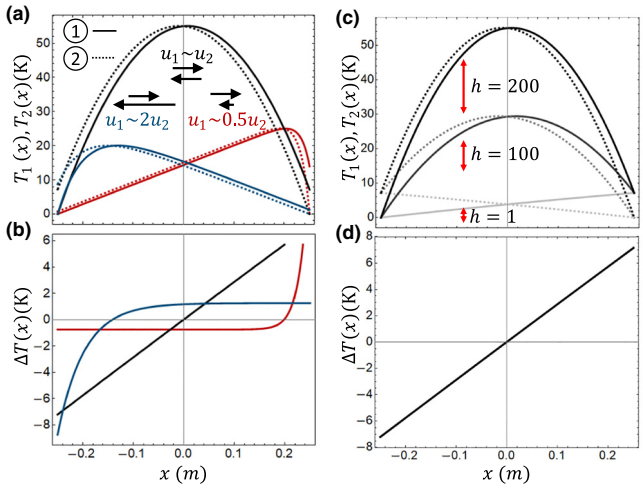

FIG. 6. (a) Temperature profiles $T_1(x)$ and $T_2(x)$ of channels 1 (solid) and 2 (dashed), respectively, for three different configurations: $u_2 \sim 2u_1$ (blue), $u_2 \sim u_1$ (black), and $u_2 \sim 0.5u_1$ (red). (b) Temperature difference between the channels $\Delta T(x) = T_1(x) - T_2(x)$ for three different configurations: $u_2 \sim 2u_1$ (blue), $u_2 \sim u_1$ (black), and $u_2 \sim 0.5u_1$ (red). $\rho = \rho_w = 1000$ kg/m^3, $c = c_w = 4.18$ kJ/kg, $I_s = 50$ W/m^2, $L = 0.5$ m, $w = 1$ mm, $u_1 = 0.83$ mm/s, and $h = 200$ W/(m^2 K). (c) Temperature profiles $T_1(x)$ and $T_2(x)$ of channels 1 (solid) and 2 (dashed), respectively, for $u_2 \sim u_1$ with $h = 1$, 100, 200 W/(m^2 K) from light to dark gray color. (d) Temperature difference profile $\Delta T(x)$ with $u_2 \sim u_1$ with $h = 1$, 100, 200 W/(m^2 K). All cases overlap. $\rho = \rho_w = 1000$ kg/m^3, $c = c_w = 4.18$ kJ/kg, $I_s = 50$ W/m^2, $L = 0.5$ m, $w = 1$ mm, $u_1 = 0.83$ mm/s, and $h = 200$ W/(m^2 K).

$T_2(x)$, can be obtained when $u_1 \sim u_2$, as shown in Fig. 6(a). Absolute temperature profiles and their difference $\Delta T(x) = T_1(x) - T_2(x)$ [Fig. 6(b)] can be tuned varying the relative velocity of the flows. Interestingly, the condition $u_1 \sim u_2$ generates a linear $\Delta T(x)$ with a change of sign at the origin, a critical ingredient of the oscillatory behavior under investigation. The dependence of the absolute temperatures evaluated at $u_1 \sim u_2 = u$, $T_{1,u}(x)$ and $T_{2,u}(x)$ on the heat-transfer coefficient h is shown in Fig. 6(c). We notice that (i) $T_{1,u}(x)$ and $T_{2,u}(x)$ depend on h and reach their maximum at $x = 0$, however their difference, $T_u(x) = (2I_S/\phi u)x$, is independent of h [Fig. 6(d)] where all lines overlap. (ii) Increasing heat-transfer coefficient h changes the temperature profiles from linear to parabolic functions. This trend is reported in Fig. 6(c) where temperatures shift from straight lines to parabolas for increasing h values.

APPENDIX E: SYSTEM LINEARIZATION AND JACOBIAN MATRIX

Restricting our analysis to the case $u_2 \sim u_1 = u$, we notice that the equation for $\dot{y}$ is already linear [$\Delta T_u(x) = (2I_S/\phi u)x$], while the expression for $\dot{x}$ needs to be simplified. First, we linearize the velocity across the interface between the channels by assuming a linear but realistic dependance [34] of $u(y)$ on y [see blue arrows in Fig. 2(d)]. In the case of a thin ($w \ll D$) and long ($w \ll L$) rectangular duct centered at $y = 0$, the velocity along x can be written as $u(y)/u_{\max} \approx [1 - (2y/w)^n]$ [34], where $u_{\max}$ is the maximum velocity in the duct. By shifting the y axis (in our case $y = 0$ is at the interface between the channels) and approximating the y dependence to the first order ($n = 1$), we can linearize, close to $y = 0$, the y dependence of the velocity with a continuous function: $u(y) = 4u(y/w)$. These assumptions are not restrictive for our analysis, as we consider the system dynamics close to the origin, which is an equilibrium point for both the nonlinear and linear systems, being $\dot{x} = f(x)y$ and $\dot{y} = \text{const} \times y$. The linearized system at the equilibrium point (0,0) can be finally obtained from

$$J = \begin{pmatrix} \frac{\partial \dot{x}}{\partial x} & \frac{\partial \dot{x}}{\partial y} \\ \frac{\partial \dot{y}}{\partial x} & \frac{\partial \dot{y}}{\partial y} \end{pmatrix} = \begin{pmatrix} \begin{cases} 4\rho c u \frac{\partial}{\partial x}\left[T_{1,u}(x)\right] y/w, & y > 0 \\ 4\rho c u \frac{\partial}{\partial x}\left[T_{2,u}(x)\right] y/w, & y < 0 \end{cases} & \begin{cases} 4\rho c u T_{1,u}(x)/w, & y > 0 \\ 4\rho c u T_{2,u}(x)/w, & y < 0 \end{cases} \\ -h_{\text{eff}} \frac{2I_S}{\phi u} & 0 \end{pmatrix}. \tag{E1}$$

By considering the Jacobian matrix, J, of the system evaluated at the equilibrium point (0,0) and $u(y) = 4u(y/w)$, we have

$$\begin{pmatrix} \dot{x} \\ \dot{y} \end{pmatrix} = J_{(0,0)} \begin{pmatrix} x \\ y \end{pmatrix}, \tag{E2}$$

with

$$J_{(0,0)} = \begin{bmatrix} 0 & \frac{I_S L}{w^2}\left(\frac{hL}{\phi u} + 2\right) \\ -h\frac{2I_S}{\phi u} & 0 \end{bmatrix}. \tag{E3}$$

APPENDIX F: COMPARISON WITH HARMONIC SYSTEMS

From linearized system we extract the complex eigenvalues:

$$\lambda_{1,2} = \pm i\omega_0 = \pm i\frac{I_s}{w}\sqrt{\frac{2hL}{\phi u}\left(\frac{hL}{\phi u}+2\right)} \tag{F1}$$

and by normalizing to I_S/w and if $hL/\phi u \gg 2$ we also have

$$|\omega_0| \propto \frac{\sqrt{2}}{\phi}h\frac{L}{u} \propto h\tau_0 \tag{F2}$$

with $\tau_0 = L/u$. ω_0 goes to zero, consistently with η_{res} approaching one [Eq. (7)], for either vanishing h or τ_0. By considering the general equation of a harmonic oscillator, our system satisfies the equation:

$$\frac{1}{b}\ddot{x} - cx = 0, \tag{F3}$$

with $b = (I_S L/w^2)\,(hL/\phi u + 2)$ and $c = -h(2I_S/\phi u)$. From this perspective $1/b$ represents the inertial term (proportional to $\phi = \rho c w$, and nonzero even when the channels do not interact, $h = 0$) and c the pulling term (proportional to h). Differently from more conventional driven oscillators, here the driving term is naturally embedded in the system itself through I_s and u but, importantly, both I_s and u can be controlled and used as external drivers.

APPENDIX G: INCREASING OSCILLATION AMPLITUDE FOR THE NONLINEAR SYSTEM

The physical reason why the oscillation amplitude increases is the following: referring to Fig. 6(c), we observe that $T_1(x)$ and $T_2(x)$ are similar but slightly shifted along x and, in fact, they give rise to the temperature difference $\Delta T_{1,2} = T_1 - T_2$ shown in Fig. 6(d). Importantly, when the heat probe switches channel ($1 \to 2$ or $2 \to 1$) the temperature of the next channel is always lower than the channel of origin. Therefore, $\dot{x}$ decreases at each switch while $\dot{y}$ stays the same as it only depends on $\Delta T_{1,2}$, which is constant along y [see Eq. (3)]. As a consequence, at each switch, the overall velocity vector becomes more parallel to y and pulls the probe away from the origin, which becomes unstable. The linearized system, being evaluated at the origin, shares the same temperature along y as $T_1(0) = T_2(0)$, and the amplitude is constant.

APPENDIX H: IMPACT OF THERMAL INERTIA AND TIME-DEPENDENT PERTURBATIONS

Flow-driven systems at resonance exhibit a large permanence time τ as shown in the main text [see Eqs. (6) and (7)]. This property (enhanced thermal inertia) translates in both an enhanced time duration of stored thermal energy (once the input power is turned off) and a longer "charging" time when the device starts its operation at room temperature. In Fig. 7 we report the average temperature increase in the water channels ($T_{\text{avg}} - T_{\text{amb}}$) versus time once the input power ($I_s = 50$ W/m^2) is turned on at $t = 0$. The relatively long stabilization time, t_s, reflects the thermal-energy accumulation dynamics, which is maximized at the resonant condition ($Q_1 = Q_2 = 5$ ml/min). The accumulation lasts for about 5 h, which is consistent with $\tau \approx 60$ min of Fig. 9(d) (case $m_{\text{loss}} = 0.001$), being $t_s \approx 5\tau$.

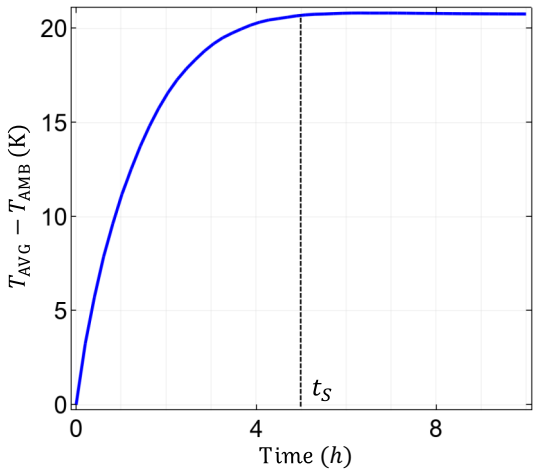

FIG. 7. Thermalization dynamics at beginning of operation. $Q_1 = Q_2 = 5$ ml/min. Input intensity $I_s = 50$ W/m^2. The value of the other parameters are detailed in Appendix I with $m_{\text{loss}} = 0.001$.

A relatively large τ also implies a relatively high robustness to fast perturbations as the device takes times of the order of τ to adapt to external stimuli. Figs. 8(a) and 8(b) show the average temperature increase versus time of a stabilized [$t = 0$ of Fig. 8(a) corresponds to the stationary solution of the system in Fig. 7, i.e., $t \gg t_s$] resonant flow-driven system affected by three thermal perturbations, of equal intensity $I_p = 10 \times I_s = 500$ W/m^2 but different duration $t_p = 0.1$, 1, 10 min and applied at the same time, 1 h after the beginning of the simulation [Fig. 8(c)]. Closer views of the three individual perturbations can be observed more clearly in Figs. 8(d)–8(f). Perturbations increase the average temperatures by approximately 25 K ($t_p = 10$ min), approximately 3 K ($t_p = 1$ min), and approximately 0.5 K ($t_p = 0.1$ min) from the stationary baseline (approximately 20.5 K). In fact, τ is independent of I_s and any perturbation with duration $t_p \ll \tau$ does not have time to stabilize. A constant input intensity of 500 W/m^2 leads to temperatures larger than 500 K in the

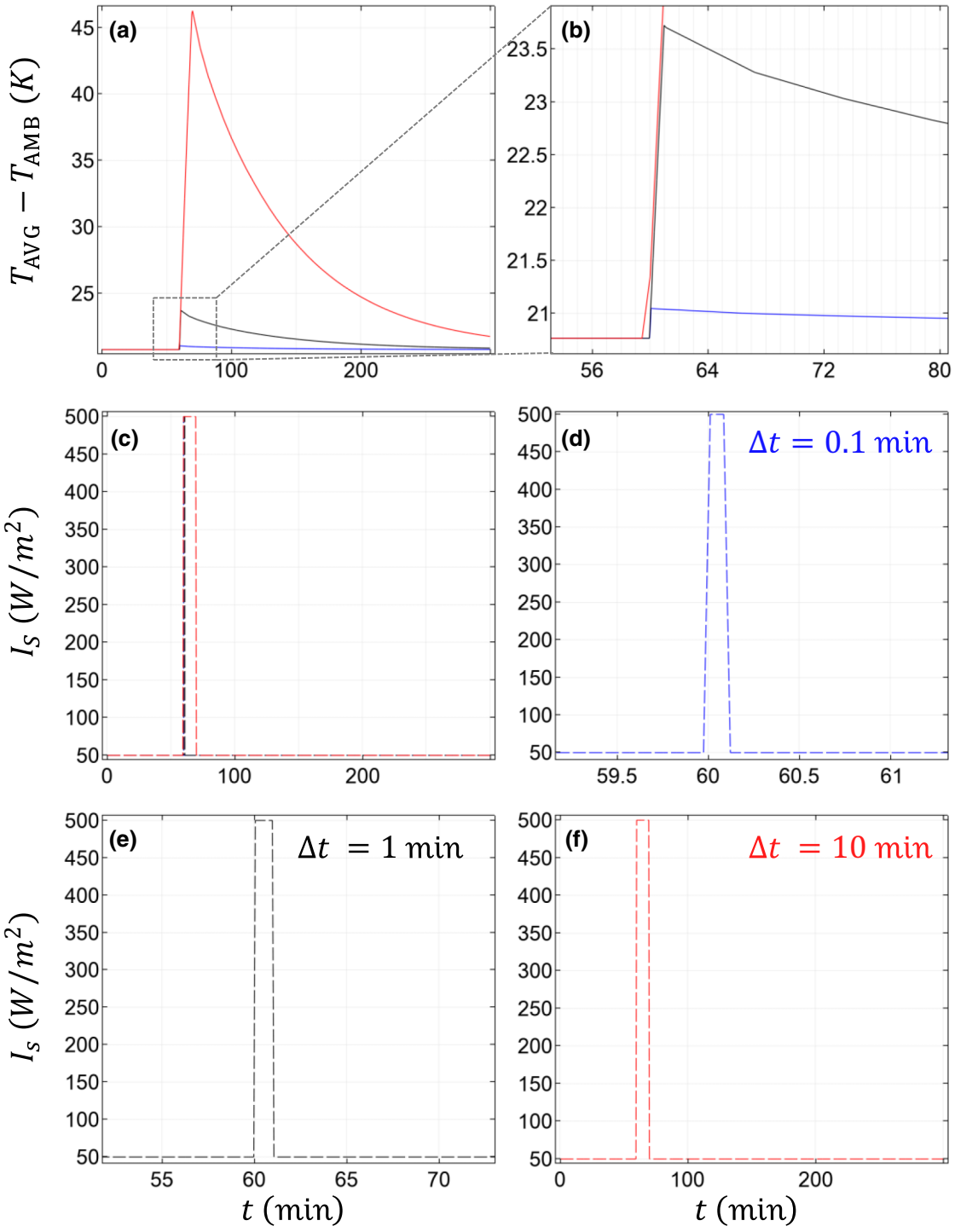

FIG. 8. Effect of perturbations on a resonant flow-driven system. (a) Average temperature increase for a stabilized system affected by a perturbation of intensity 500 W/m^2 at $t = 60$ min of different durations: 0.1 min (blue), 1 min (black), and 10 min (red). (b) Close-up view of (a). (c) Time-dependent intensity profile of the system power input. The baseline refers to $I_s = 50$ W/m^2, the thin rectangular regions show the magnitude of the perturbation $I_p = 500$ W/m^2. (d)–(f) Close-up views of the individual perturbations.

current system (if one assumes a sufficient mechanical stability at increased pressures to avoid boiling) but that takes a time approximately t_s. If perturbations last for shorter times (e.g., $t_p \ll t_s$ as shown here) their impact on the short-term temperature increase and long-term effects are limited.

APPENDIX I: IMPACT OF LOSSES IN REALISTIC SYSTEMS

To demonstrate the validity of the presented analytical approach, we employ 2D numerical calculations for the realistic representation of a resonant thermofluidic system [Fig. 9(a)]. In line with the coupled channels analyzed so far, we consider the system shown in Fig. 5 where water channels are now separated by a $t_{HX} = 100$ μm thick conductive layer with thermal conductivity $k_{HX} = 400$ W/(m K). The layer is assumed to be light absorbing with an absorption coefficient $\alpha \cong 5.81 \times 10^4$ m^{-1}. These optothermal properties are consistent, for example, with carbon black nanoparticles placed on a surface. An incident electromagnetic radiation is assumed to be vertically dissipated along y, according to a typical Lambert-Beer profile, $I_s(y)$. Additional environmental losses, Γ_{env} (conduction + convection and thermal radiation), are taken into account through a combined heat-transfer coefficient $h = 5$ W/(m^2 K) and a black-body emissivity $\epsilon_{rad} = 1$. The thermal problem is coupled with Navier-Stokes equations, assuming a laminar fluid. Water temperature-dependent thermal parameters are taken into account and utilized values can be found in Ref. [35]. Similarly to Fig. 2(b), in Fig. 9(b) we report the average temperature increase in the system by varying the flow-rate ratio Q_2/Q_1. We observe that the trend obtained analytically is well recovered, especially when external losses are low (a multiplicative factor m_{loss} has been introduced for h_{coeff} and ϵ_{rad}). When $Q_2/Q_1 \sim 1$, the previously introduced resonant condition is achieved. We also report the heat-probe trajectory,

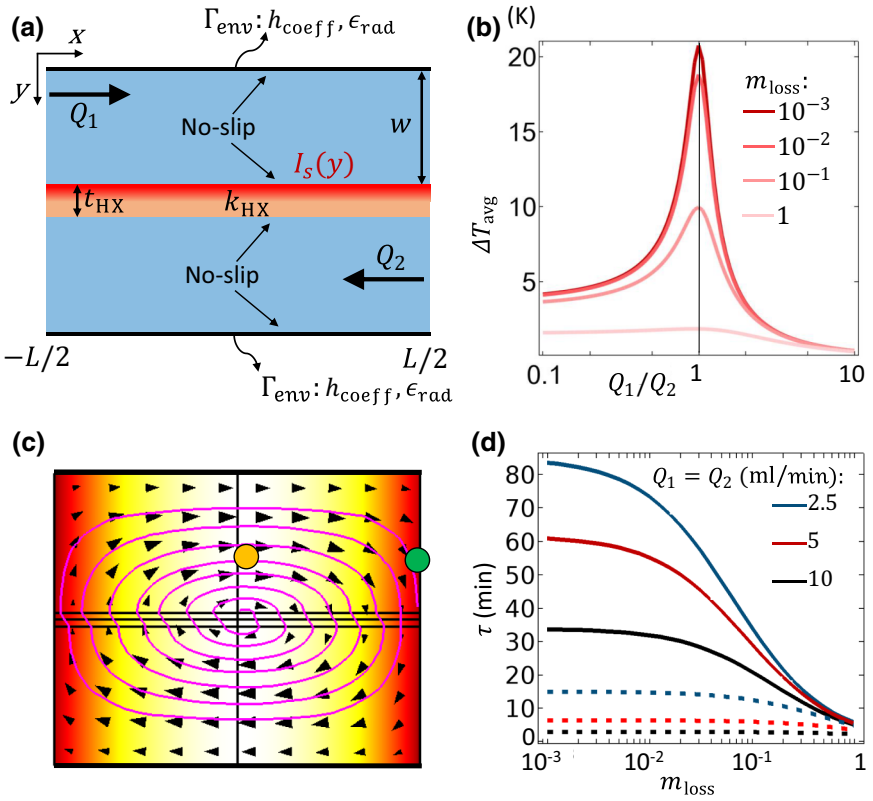

FIG. 9. (a) Realistic representation of the same system of Fig. 2(a) taking now into account: a nonzero thickness, $t_{HX} = 100$ μm, of the separation layer (heat exchanger, HX) between the channels characterized by a thermal conductivity $k_{HX} = 400$ W/(m K). Input heat source is assumed to decay exponentially along y with an absorption coefficient of 5.81×10^4 m^{-1}. Temperature-dependent density, $\rho(T)$, specific heat, $c(T)$, and fluid thermal conductivity, $k(T)$, of water are considered. No-slip boundary conditions are applied at the HX and outer boundaries of the channels. External heat-transfer coefficient, $h_{coeff} = 5$ W/(m^2 K), and black-body emissivity, $\epsilon = 1$, are imposed at the channels' boundaries to account for combined conductive and convective and radiative losses, respectively. $L = 0.5$ m, $w = 1$ mm, $Q_1 = 5$ ml/min. Channels are assumed to be $d = 4$ in $\cong 10.1$ cm wide [$u_1 = Q_1/(dw)$]. Ambient temperature is 20 °C. (b) Maximum temperature increase in the system for varying Q_2/Q_1 ratio and different loss coefficients, m_{loss}, from 1 to 10^{-3} in scale of reds. (c) Temperature map (color) and probe trajectory (magenta) dragged by heat-flux vector field (black arrowheads) for $Q_2/Q_1 \sim 1$. Dark yellow and green circles represent the initial and final coordinates of the probe at $t = 0$ and upon leaving the system, respectively. (d) Average thermal energy increases permanence time dependence on losses at different values of $Q_1 = Q_2$: 2.5 ml/min (blue), 5 ml/min (red), and 10 ml/min (black) in the case of interacting (conductive interface, solid line) and noninteracting channels (insulating interface, dotted line).

in Fig. 9(c), for $Q_2/Q_1 \sim 1$ and $m_{\text{loss}} = 1 \times 10^{-3}$, showing an outward spiral, as expected. The decay time, τ, is numerically extracted from the temperature maps. In Fig. 9(d) we report τ_{res} vs m_{loss} for three different matched flow rates, both when the channels interact [$k_{\text{HX}} = 400$ W/(m K), solid lines] and when they are almost independent [$k_{\text{HX}} = 4 \times 10^{-4}$ W/(m K), dotted lines]. The decay time enhancement is clearly observed, particularly for low losses, consistently with our theoretical analysis.

APPENDIX J: IMPACT OF FLUID THERMAL CONDUCTIVITY

Larger fluid thermal conductivities increase the heat transfer between the channels but also facilitate the vertical and horizontal diffusive heat propagation within and along the channels, respectively. Both these extra diffusive terms increase losses, pulling heat fluxes closer to the external boundaries (where heat can be exchanged with the environment) and outlets (where heat can directly exit the system). Overall, an optimal thermal conductivity, which maximizes the stored thermal energy may exist. To illustrate the concept, in Fig. 10 we show, for the system considered in this work at resonance ($Q_1 = Q_2 = 5$ ml/min), the average temperature rise for increasing thermal conductivities of the liquid filling the channels (the other thermophysical properties are kept constant and equal to the water ones). A maximum exists at around approximately 2.4 W/(m K). Thermal conductivities of water and a liquid metal (Galinstan) are highlighted.

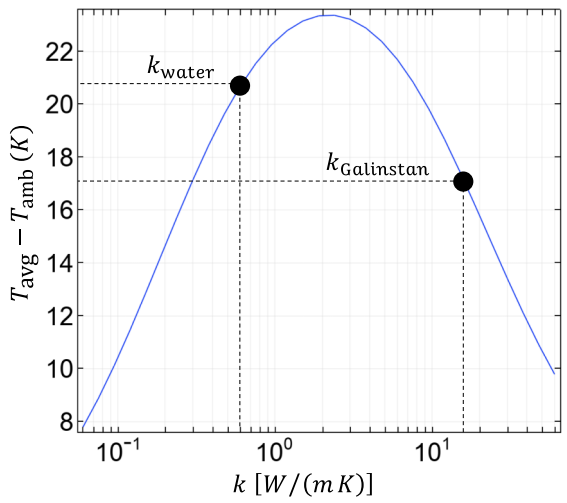

FIG. 10. Effect of fluid thermal conductivity. Average steady-state temperature increase for the system as Fig. 9 (steady-state unperturbed case) versus thermal conductivity of the fluids. The case of water [$k \sim 0.6$ W/(m K)] and a liquid metal Galinstan [$k \sim 16.5$ W/(m K)] are shown. All thermophysical properties except thermal conductivity are the same as water.

APPENDIX K: WATER AND GALINSTAN CASES

Liquid metals, besides thermal conductivity, may have different thermophysical properties from water (in particular, density, specific heat, and dynamic viscosity) and could be potential candidates for thermal-storage applications based on flow-driven resonant systems. In Fig. 11 we show the maximum temperature increase in the resonant system versus increasing matched fluid flows for the case of water (blue) and Galinstan (red). Two extreme loss coefficients are considered [$m_{\text{loss}} = 1$ (solid) and $m_{\text{loss}} = 0.001$ (dashed)]. The same numerical calculations are performed for the case of a system of length 0.5 m [Fig. 11(a)] and 2.5 m [Fig. 11(b)]. In Fig. 11(a) we see that for small fluid flow rates there is not a big advantage of a fluid over the other, in terms of temperature increase (and thus thermal storage). However, if we consider larger devices the properties of

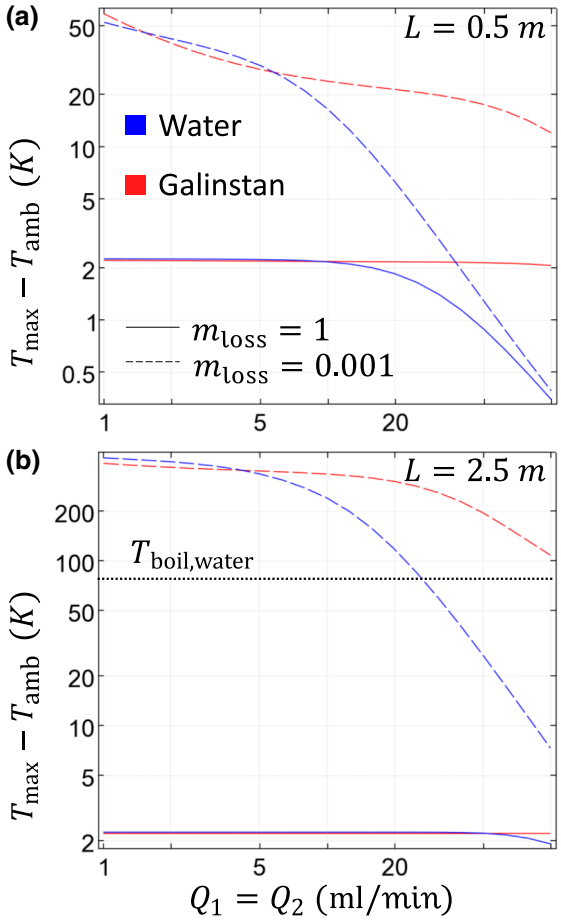

FIG. 11. Water and Galinstan case. Maximum temperature increase in the system (same parameters as Fig. 10) versus matched fluid flows in the case of water (blue) and Galinstan (red) for different loss coefficients $m_{\text{loss}} = 1$ (solid) and $m_{\text{loss}} = 0.001$ (dashed). For Galinstan, the following parameters have been considered: density 6.44 g/cm^3, dynamic viscosity 0.0024 Pa s, specific heat 296 J/(kg K), thermal conductivity 16.5 W/(m K). Scales are logarithmic.

liquid metals could be advantageous. Figure 11(b) shows the maximum temperature increase for a 2.5 m system. At larger flow rates Galinstan performs better, especially for small losses. More importantly, for slower flows, the boiling point of water would be easily reached in the case of $m_{\text{loss}} = 0.001$, hindering the mechanical stability of the device if room pressure operation is sought. However, Galinstan has a high boiling point (> 1300 °C), and thus one can think of storing thermal energy by realizing larger systems and feeding them with slower flow rates without risking reaching the boiling point of the utilized fluid.

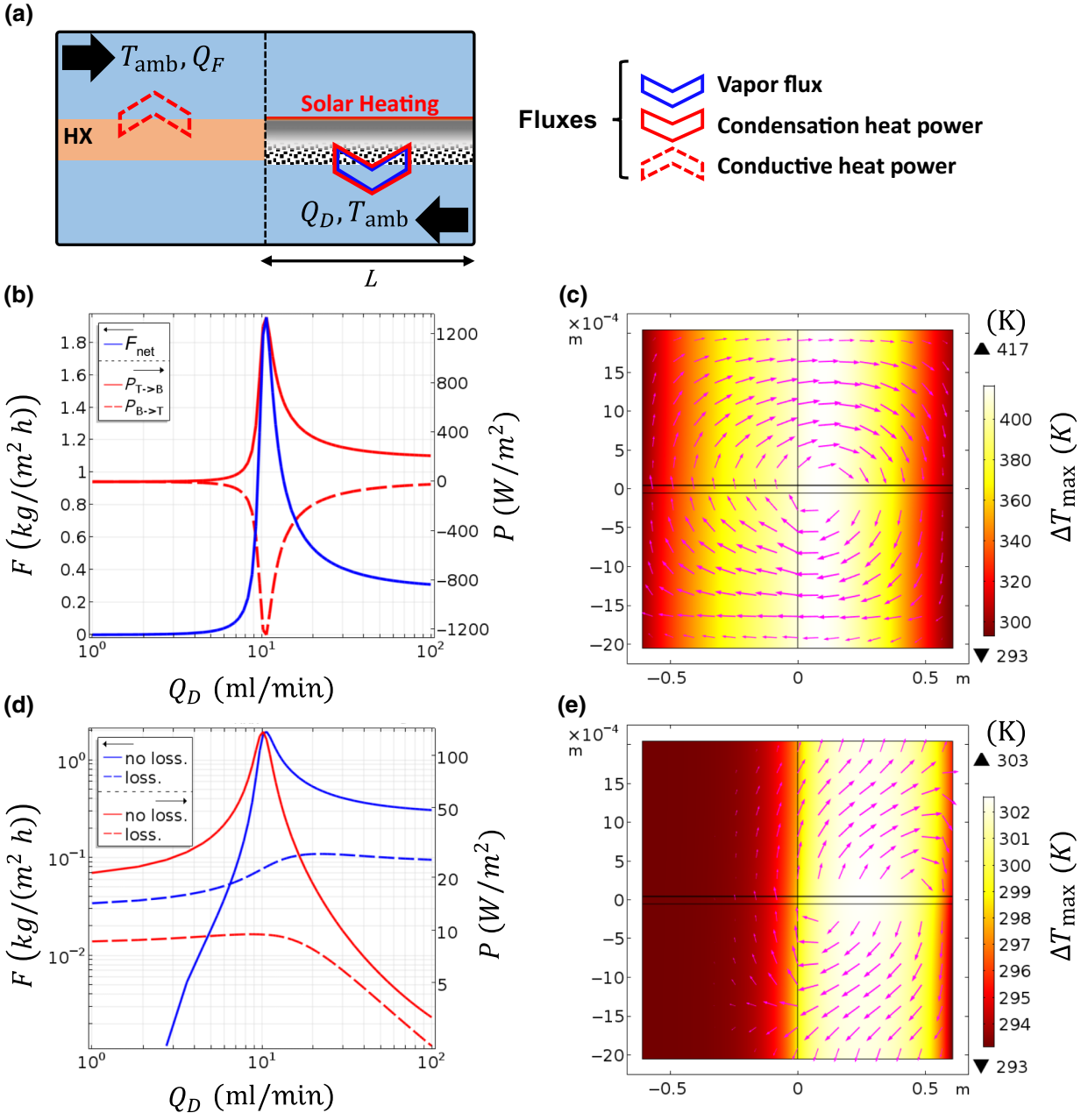

FIG. 12. Application to solar water desalination. (a) Saline feed water (Q_F) and distilled water (Q_D) flow in the top and bottom channel, respectively, upon entering the resonant system at ambient temperature, T_{amb}. Channels are separated by a thermal conductor (first half, left) and a light-absorbing nanoparticle-coated hydrophobic membrane (second half, right). Input intensity is 269 W/m^2. (b) Fresh-water flux (blue, left axis) across the membrane and heat fluxes (right axis) from top to bottom, $P_{T\to B}$, (solid, red) and bottom to top, $P_{B\to T}$, (dashed, red) versus distillate flow rate. Feed flow is fixed at 10 ml/min. (c) Heat-flux vector fields (arrows) and temperature map (colors) when the flow rates are matched for a lossless case. (d),(e) Same as (b),(c), but in the case of external environmental losses ($P_{T\to B}$ case shown only in red): conduction+convection [$h_{\text{coeff}} = 5$ W/(m^2 K)] and thermal radiation ($\epsilon = 1$) are applied to the top and bottom boundaries of feed and distillate channels.

APPENDIX L: EXAMPLE OF APPLICATION: SOLAR THERMAL DESALINATION

One application of flow-driven resonant systems is solar desalination and resonant energy transfer for thermal membrane distillation has been recently demonstrated [9]. In nanoparticle- (NP) driven solar membrane desalination [31], two water channels, feed (saline) and distillate (fresh water), flow in countercurrent configuration, separated by a hydrophobic membrane (100 μm thick) which allows water vapor but not liquid water to go through. Such a membrane can be coated, on the feed side, with efficient light-absorbing nanoparticles (e.g., carbon black NPs), which absorb more than 99% in about 10 μm thickness. The heat generated in the NPs induces a vapor-pressure difference across the membrane, pushing salt-free water vapor from the feed side of the membrane to the distillate one.

The key idea is to recognize that the latent heat of condensation carried by water vapor across the membrane can represent the downward heat flux (I_{12} in the main text), which can be recovered by placing a thermal conductor (acting as heat exchanger, HX) in line with the membrane [see Fig. 12(a)]. The conductive heat recovered with the HX is then reused to further increase the feed water temperature and increase even more the vapor-pressure difference. The process at this point is limited only by the thermal losses of the system and by the boiling temperature of water (if water starts boiling the pressure can increase and the membrane can wet, hindering the mechanical stability of the system and the water impermeability between the channels). In Fig. 12(b) we show the fresh-water flux rate (blue line) versus distillate flow rate when the feed flow is fixed at 10 ml/min for the case of a $L = 0.6$ m membrane in line with an aluminum HX of the same length, without environmental losses (i.e., convection and thermal radiation). Incident intensity is 269 W/m^2 (approximately 0.27 Suns). The heat fluxes from top to bottom (solid, red) and bottom to top (solid, dashed) are also shown. All the curves exhibit a clear peak when flows are matched, consistently with the theoretical model explained in this work. The heat-flux vector field is reported in Fig. 12(c) and well matches the trajectories explained in the main text (e.g., Fig. 3). The peak temperature is larger than water boiling point but here, for simplicity, we neglect its effects since this lossless example is presented only to illustrate the concept of resonant heat transfer in the ideal lossless case. The impact of losses is shown in Figs. 12(d) and 12(e). When external conduction+convection [combined heat transfer coefficient $h_{\text{coeff}} = 5$ W/(m^2 K)] and thermal radiation ($\epsilon = 1$) are added at the top and bottom boundaries of the channels, the performance (and the peak temperature) decreases quite steeply and the vector field is deformed. This result suggests the critical importance of the choice of materials, which should provide a maximum insulation to ensure loss minimization. Aerogels and infrared mirrors can be utilized, for instance, to decrease convection and radiation losses.

ADDITIONAL INFORMATION

A provisional patent application has been submitted in relation to the research.

[1] G. Karakostas and Y. Wu, Nonlinear analysis: Theory, Methods & Applications **20**, 269 (1993).

[2] H. Karttunen, P. Kröger, H. Oja, M. Poutanen, and K. J. Donner, *Fundamental Astronomy* (Springer Berlin Heidelberg, New York, 2016).

[3] A. T. Winfree, *The Geometry of Biological Time* (Springer, New York, 2001).

[4] G. Buzsaki, *Rhythms of the Brain* (Oxford University Press, New York, 2006).

[5] J. D. Jackson, *Classical Electrodynamics* (John Wiley & Sons, USA, 1999), 3rd ed.

[6] M. K. Kazimierczuk and D. Czarkowski, *Resonant Power Converters* (Wiley, Hoboken, N.J., 2012).

[7] S. J. Oldenburg, R. D. Averitt, S. L. Westcott, and N. J. Halas, Nanoengineering of optical resonances, Chem. Phys. Lett. **288**, 243 (1998).

[8] S. Etaki, M. Poot, I. Mahboob, K. Onomitsu, H. Yamaguchi, and H. S. J. van der Zant, Motion detection of a micromechanical resonator embedded in a d.c. SQUID, Nat. Phys. **4**, 785 (2008).

[9] A. Alabastri, P. D. Dongare, O. Neumann, J. Metz, I. Adebiyi, P. Nordlander, and N. J. Halas, Resonant energy transfer enhances solar thermal desalination, Energy Environ. Sci. **13**, 968 (2020).

[10] S. H. a. Strogatz, *Nonlinear Dynamics and Chaos: with Applications to Physics, Biology, Chemistry, and Engineering* (Westview Press, Boulder, CO: a member of the Perseus Books Group, [2015], 2015), 2nd ed.

[11] M. J. Clifford and S. R. Bishop, Rotating periodic orbits of the parametrically excited pendulum, Phys. Lett. A **201**, 191 (1995).

[12] V. Volterra, Fluctuations in the abundance of a species considered mathematically, Nature **118**, 558 (1926).

[13] S. H. Strogatz, Love affairs and differential equations, Mathematics Magazine **61**, 35 (1988).

[14] F. Dercole and S. Rinaldi, Love stories can be unpredictable: Jules et Jim in the vortex of life, Chaos **24**, 023134 (2014).

[15] S. A. Maier, *Plasmonics: Fundamentals and Applications* (Springer, USA, 2007).

[16] C.-P. Huang, X.-P. Yin, H. Huang, and Y.-Y. Zhu, Study of plasmon resonance in a gold nanorod with an LC circuit model, Opt. Express **17**, 6407 (2009).

[17] W. F. Pickard and B. Abraham-Shrauner, Simplified models of the symmetric single-pass parallel-plate counterflow heat exchanger: A tutorial, R. Soc. Open Sci. **5**, 171617 (2018).

[18] S. Kakac, H. Liu, and A. Pramunjaroenkij, *Heat Exchangers: Selection, Rating, and Thermal Design* (CRC Press, Boca Raton, FL, 2012), 3rd ed.

[19] M. Vera and A. Liñàn, Laminar counterflow parallel-plate heat exchangers: Exact and approximate solutions, Int. J. Heat Mass Transfer **53**, 4885 (2010).
[20] V. W. Kotiaho, Thermal analysis of a counterflow heat exchanger with a heat source, Int. J. Ambient Energy **31**, 211 (2010).
[21] L. H. V. T. A. Ameel, Countercurrent heat exchangers with both fluids subjected to external heating, Heat Transfer Eng. **20**, 37 (1999).
[22] J. Swaminathan, H. W. Chung, D. M. Warsinger, and J. H. Lienhard V, Membrane distillation model based on heat exchanger theory and configuration comparison, Appl. Energy **184**, 491 (2016).
[23] J. Swaminathan, H. W. Chung, D. M. Warsinger, and J. H. Lienhard V, Simple method for balancing direct contact membrane distillation, Desalination **383**, 53 (2016).
[24] S. Lin, N. Y. Yip, and M. Elimelech, Direct contact membrane distillation with heat recovery: Thermodynamic insights from module scale modeling, J. Membr. Sci. **453**, 498 (2014).
[25] L. Zhou et al., Quantifying hot carrier and thermal contributions in plasmonic photocatalysis, Science (Washington, DC, U. S.) **362**, 69 (2018).
[26] E. Chiavazzo, M. Morciano, F. Viglino, M. Fasano, and P. Asinari, Passive solar high-yield seawater desalination by modular and low-cost distillation, Nat. Sustain. **1**, 763 (2018).
[27] A. O. Govorov and H. H. Richardson, Generating heat with metal nanoparticles, Nano Today **2**, 30 (2007).
[28] G. Baffou and R. Quidant, Thermo-plasmonics: Using metallic nanostructures as nano-sources of heat, Laser Photonics Rev. **7**, 171 (2013).
[29] A. Alabastri, M. Malerba, E. Calandrini, A. Manjavacas, F. De Angelis, A. Toma, and R. Proietti Zaccaria, Controlling the heat dissipation in temperature-matched plasmonic nanostructures, Nano Lett. **17**, 5472 (2017).
[30] A. Politano, P. Argurio, G. Di Profio, V. Sanna, A. Cupolillo, S. Chakraborty, H. A. Arafat, and E. Curcio, Photothermal membrane distillation for seawater desalination, Adv. Mater. **29**, 1603504 (2017).
[31] P. D. Dongare, A. Alabastri, S. Pedersen, K. R. Zodrow, N. J. Hogan, O. Neumann, J. Wu, T. Wang, A. Deshmukh, M. Elimelech, Q. Li, P. Nordlander, and N. J. Halas, Nanophotonics-enabled solar membrane distillation for off-grid water purification, Proc. Natl. Acad. Sci. **114**, 27 (2017).
[32] B. Bird, W. Stewart, and E. Lightfoot, *Transport Phenomena* (John Wiley & Sons, Inc., 2006), Revised 2nd ed.
[33] I. Dincer and C. Zamfirescu, in *Drying Phenomena: Theory and Applications* (John Wiley & Sons, Ltd., 2016).
[34] R. K. Shah, *Laminar Flow Forced Convection in Ducts: A Source Book for Compact Heat Exchanger Analytical Data* (Academic Press, New York, 1978).
[35] P. D. Dongare, A. Alabastri, O. Neumann, J. Metz, I. Adebiyi, P. Nordlander, and N. J. Halas, Solar thermal desalination as a nonlinear optical process, Proc. Natl. Acad. Sci. **116**, 27 (2019).